Structural and vibrational study of $Zn(IO_3)_2$ combining high-pressure experiments and density-functional theory

A. Liang,[1] C. Popescu,[2] F. J. Manjon,[3] P. Rodriguez-Hernandez,[4] A. Muñoz,[4] Z. Hebboul,[5] and D. Errandonea[1]

[1]*Departamento de Física Aplicada-ICMUV-MALTA Consolider Team, Universitat de València, c/Dr. Moliner 50, 46100 Burjassot (Valencia), Spain*

[2]*CELLS-ALBA Synchrotron Light Facility, Cerdanyola del Vallès, 08290 Barcelona, Spain*

[3]*Instituto de Diseño para la Fabricación y Producción Automatizada, MALTA Consolider Team, Universitat Politècnica de València, Camí de Vera s/n, 46022 València, Spain*

[4]*Departamento de Física and Instituto de Materiales y Nanotecnología, MALTA Consolider Team, Universidad de La Laguna, 38206 La Laguna, Tenerife, Spain*

[5]*Laboratoire Physico-Chimie des Matériaux (LPCM), University Amar Telidji of Laghouat, BP 37G, Ghardaïa Road, Laghouat 03000, Algeria*

(Received 16 November 2020; revised 24 January 2021; accepted 26 January 2021; published 2 February 2021)

We report a characterization of the high-pressure behavior of zinc iodate, $Zn(IO_3)_2$. By the combination of x-ray diffraction, Raman spectroscopy, and first-principles calculations we have found evidence of two subtle isosymmetric structural phase transitions. We present arguments relating these transitions to a nonlinear behavior of phonons and changes induced by pressure on the coordination sphere of the iodine atoms. This fact is explained as a consequence of the formation of metavalent bonding at high pressure which is favored by the lone-electron pairs of iodine. In addition, the pressure dependence of unit-cell parameters, volume, and bond distances is reported. An equation of state to describe the pressure dependence of the volume is presented, indicating that $Zn(IO_3)_2$ is the most compressible iodate among those studied up to now. Finally, phonon frequencies are reported together with their symmetry assignment and pressure dependence.

DOI: 10.1103/PhysRevB.103.054102

I. INTRODUCTION

Metal iodates form a group of materials that have been intensively studied as promising nonlinear optics (NLO) materials [1–3] in the visible-, near-, and midinfrared (IR) ranges of the electromagnetic spectrum. Moreover, recent density-functional theory (DFT) calculations reveal that metal iodates exhibit large or even giant elastocaloric (EC) effect, which made them promising materials for developing solid-state cooling technologies [4,5]. These materials are of interest also for fundamental research owing to the presence of stereochemically active lone electron pairs (LEPs) on iodine atoms.

Of special interest are the studies of the crystal structure and vibration behavior of metal iodates at high pressure (HP). Recently, we have reported a comprehensive crystal structure and vibration study of $Fe(IO_3)_3$ under compression employing x-ray diffraction, IR spectroscopy, Raman scattering (RS) measurements, and first-principles DFT calculations [6,7]. Three isostructural phase transitions (IPTs) were found at 1.5, 5.7, and 22 GPa, respectively. The first two transitions do not involve detectable discontinuities in the unit-cell volume, but the third transition has associated a large volume collapse, being a first-order transition. The sequence of transformations is accompanied by a gradual increase of iodine (I) coordination from three to six [6]. The rich phase transition sequence and coordination change is mostly due to changes associated with the LEPs of I atoms [7]. As we have demonstrated in the previous HP-study of $Fe(IO_3)_3$, iodates seem to exhibit many unusual and interesting properties and changes at HP [6,7]. However, until now, except for $Fe(IO_3)_3$, only the behavior of the crystal structure of $LiIO_3$ [8–10], KIO_3 [11], and $AgIO_3$ [12] has been studied at HP. This does not include other properties, such as lattice vibrations, electronic density of states, and electronic band structure. For $Zn(IO_3)_2$, its crystal structure [13–15], Raman and IR spectrum [16,17] have been well studied at ambient conditions, but research at HP is not available.

Here we extend the HP study on another metal iodate, $Zn(IO_3)_2$. At ambient conditions, $Zn(IO_3)_2$ crystallizes in a monoclinic structure (space group: $P2_1$, $Z = 4$) [15], which is shown in Fig. 1. In this structure ZnO_6 octahedral units are bridged by IO_3 triangular pyramids (see Fig. 1). In the IO_3^- anion, iodine, with a valence configuration $5s^25p^5$, is pentavalent and forms three covalent bonds with oxygen by sharing its p electrons, leaving the 5 s electrons free to orient along the c axis, showing an IO_3E configuration, E being the LEP. This characteristic of the IO_3^- anion triggers an interesting and unusual behavior in $Fe(IO_3)_3$ at HP [6,7,11,12]. Apart from that, the LEP-induced anharmonicity can provide an efficient way to minimize the lattice thermal conductivity [18,19]. These characteristics are shared by the crystal structures of $Zn(IO_3)_2$ and $Fe(IO_3)_3$, which suggests that $Zn(IO_3)_3$ could potentially have a quite interesting EC effect at HP.

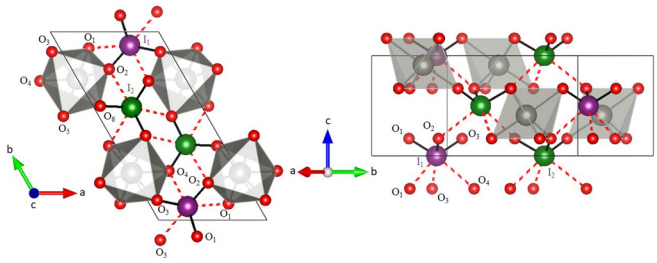

FIG. 1. Crystal structure of $Zn(IO_3)_2$ at ambient conditions. (a) Schematic crystal structure projected onto *ab* plane and (b) in a perspective where all iodine atoms in the unit cell can be seen. I atoms are shown in purple (I_1) and green (I_2) color. The Zn coordination octahedral units are shown in gray. O atoms are shown in red and have been labeled. First-neighbor I-O bonds are shown with solid black lines and second-neighbor I-O bonds are shown with red dashed lines. First-neighbor O atoms of Zn have been labeled in one octahedron. First and second neighbors of I_1 have also been labeled for the I_1 atom in the bottom part of the structure.

In this paper, HP x-ray diffraction (HP-XRD), HP Raman scattering (HP-RS), and DFT calculations have been used to investigate the HP behavior of $Zn(IO_3)_2$. Two symmetry-preserving phase transitions have been found. Their existence has been related to changes found in the iodine atom coordination. We have also observed the existence of soft-phonon modes, which have been found in the high-frequency range in HP-RS studies. These vibrations have been associated with the vibration behavior of I-O bonds. All of the experimental data will be compared with DFT simulations, giving a deep insight into the structural and vibrational behavior of $Zn(IO_3)_2$ under pressure.

II. METHODS

A. Sample preparation

For the study of $Zn(IO_3)_2$, micrometer-sized needlelike crystals were synthesized from an aqueous solution [20]. $Zn(IO_3)_2$ was prepared by mixture of potassium iodate KIO_3 (2 mmol, 99.5% purity) and zinc chloride $ZnCl_2$ (1 mmol, 98% purity) in deionized water: $2KIO_3 + ZnCl_2 \rightarrow Zn(IO_3)_2 + 2KCl$. The reagents were purchased from Fluka (KIO_3) and Riedel-deHeän ($ZnCl_2$). The reaction mixtures were slowly evaporated and maintained at 60 °C for 4 d, leading to the formation of white precipitations. We filtrated and washed the crystals with deionized water.

To confirm the purity and crystal structure of $Zn(IO_3)_2$, we performed powder XRD measurements at room conditions (see Fig. 2) using an XPERT Pro diffractometer from Panalytical in a reflection Bragg-Brentano geometry and employing monochromatic Cu $K_{\alpha 1}$ radiation. The Rietveld refinement method [21] was adopted to analyze the phase and lattice parameter information. The structural information of $Zn(IO_3)_2$ reported by Liang *et al.* [15] (space group $P2_1$) was used as a starting point to do the refinement. We have found in the refinement that all the peak positions match very well and that the intensity of most peaks agrees with those already reported except for some peaks between 30°–50° due to the partially preferred direction of the needle-shaped sample. The

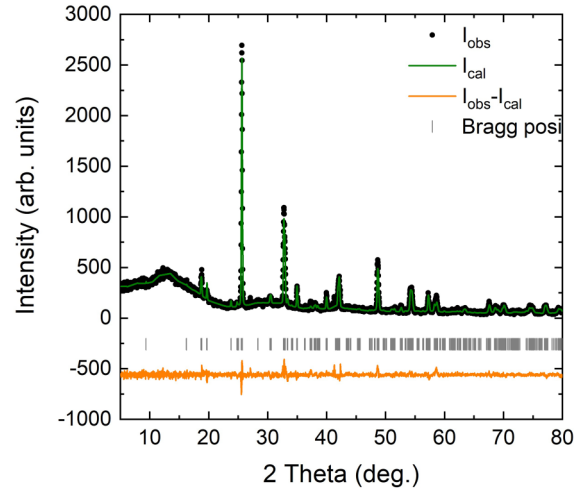

FIG. 2. XRD pattern measured at ambient pressure (circles). The green line is the Rietveld refinement. The quality factors of Rietveld refinement are $R_p = 7.22\%$ and $R_{wp} = 9.91\%$. Residuals are shown in orange.

lattice parameters obtained from our refinements and DFT calculations are listed in Table I and compared with the values reported in the literature [15]. The atomic positions are given in the Supplemental Material (Table S1) [22]. The agreement regarding unit-cell parameters is good, differences between experiments and calculations being within 1%.

B. High-pressure experiment details

Angle-dispersive powder HP-XRD experiments were performed at room temperature up to 27.8 GPa employing a membrane diamond-anvil cell (DAC), with diamond culets of 400 μm. For these experiments the $Zn(IO_3)_2$ sample was grinded to obtain a micrometer-size powder which was loaded in a 180-μm-diameter hole drilled on a stainless-steel gasket preindented to a thickness of 40 μm. We paid special attention to occupy with the sample a small fraction of the gasket hole to prevent the sample bridging between the diamond culets because of the thinning of the gasket under compression. Pressure was measured using the equation of state of gold [23] and a 16:3:1 methanol:ethanol-water mixture was used as the pressure-transmitting medium (PTM) [24]. Experiments were performed at the BL04-MSPD of ALBA synchrotron [25]

TABLE I. Summary of the lattice parameters and volume, V_0, of $Zn(IO_3)_2$ at ambient pressure from calculations (DFT) and experiments (Exp.). Previous experimental data from Ref. [15] are also included for comparison.

	DFT[a]	Exp.[a]	Exp. [15]
a (Å)	5.469	5.465(4)	5.469
b (Å)	10.832	10.952(8)	10.938
c (Å)	5.054	5.129(4)	5.1158
γ (°)	120.514	120.37(8)	120.000
V_0 (Å^3)	258.00	264.8(4)	265.03

[a]This work,

with a monochromatic x-ray beam ($\lambda = 0.4246$ Å) focused to a 20-μm × 20-μm full with at half maximum spot.

HP-RS measurements were performed in $Zn(IO_3)_2$ needle-shaped crystals also with a DAC, where sample and ruby chips were loaded in the 150-μm-diameter hole of a preindented steel gasket. Based upon the results of HP XRD studies (which showed that phase transitions occur below 10 GPa as we will discuss in the next section) Raman studies were limited to 12 GPa. Again a 16:3:1 mixture was used as PTM [24]. Pressure was determined using the ruby fluorescence scale [26]. We paid special attention during sample loading to avoid the hydration of the metal iodates [27]. We also made a careful loading avoiding sample bridging between diamond anvils [28]. Measurements were performed in a backscattering geometry employing a HeNe laser (632.8 nm) with a 10-mW power and a HORIBA Jobin Yvon LabRAM HR UV microspectrometer with a spectral resolution better than 2 cm^{-1}.

C. *Ab initio* simulations

Calculations of the total energy as a function of pressure for $Zn(IO_3)_2$ were performed using the Vienna *Ab initio* simulations package (VASP) [29–32] within the framework of the density functional theory [33] and the projector-augmented wave pseudopotential method [34,35]. A high plane-wave energy cutoff of 540 eV was used to obtain accurate results. The exchange-correlation energy was described within the generalized gradient approximation (GGA) with the Perdew–Burke-Ernzerhof (PBE) for solids prescription (PBESOL) [36]. The Monkhorst-Pack scheme [37] was employed to discretize the Brillouin-zone (BZ) integrations with a $4 \times 8 \times 4$ mesh to ensure accuracy. We tested that this mesh is sufficient to avoid all nonsystematic discretization errors.

With this procedure, very high convergences of 1 meV per formula unit in the total energy are achieved and in the optimized configurations, the forces are lower than 2 meV/Å per atom and the deviation of the stress tensor from a diagonal hydrostatic form is less than 0.1 GPa. All the structural parameters were obtained at selected optimized volumes. The agreement of the calculations with experiments regarding the crystal structure (within 1%, see Table II), supports that our DFT calculations properly describe $Zn(IO_3)_2$.

After optimizing the crystal structure at different pressures, a study of the phonons was performed at the zone center (Γ point) of the BZ using the direct method [38]. These calculations also allow identifying the symmetry and eigenvectors of the phonon modes at the Γ point.

III. RESULTS AND DISCUSSION

A. Structural study

Figure 3 shows HP-XRD patterns of $Zn(IO_3)_2$ at selected pressures. At the lowest pressure, all of the peaks can be assigned to the monoclinic structure we described above. Some peaks, like (120) and (041) peaks, show a relative intensity change with increasing pressure. This is due to preferred orientations related to the needle-shaped sample. We must note that preferred orientations were present at ambient pressure and become more obvious as pressure increases. From ambient to the highest pressure, all the XRD patterns can be identified in the same space group. Since Fig. 3 shows only a selection of pressures, in the Supplemental Material [22] we include a figure (Fig. S1) with multiple XRD patterns to illustrate in more detail the gradual evolution of XRD patterns with no qualitative changes in the whole pressure range covered by experiments. However, as we will discuss below we will show that subtle changes observed in the pressure evolution of lattice parameters suggest the existence of isosymmetric structural phase transitions. The changes induced by pressure in XRD patterns are reversible as can be seen in Fig. 3 in the XRD pattern measured at ambient pressure after the decompression process.

Under compression, most diffraction peaks shift to higher angles, as expected [39]. However, some peaks, like (100), (120), and $(3\bar{4}1)$, have a different behavior. In particular, the d-spacing (see Fig. S2 in Supplemental Material [22]) of the above-mentioned peaks first increases with pressure and then remain almost unchanged or reduce to a very small extent. Moreover, it must be noticed that d-spacings of $(hk0)$ peaks change much less than the (hkl) peaks with $l \neq 0$. Lattice planes like (001), $(1\bar{1}1)$, (101), (002), and (102) have a high-pressure dependence comparable to other lattice planes. Therefore, we can ascribe the different shift rates of the XRD peaks, and even the opposite shifts of some peaks, to the anisotropic compressibility of $Zn(IO_3)_2$ which we will discuss in detail later. Another consequence of the anisotropic compression of $Zn(IO_3)_2$ is the merging and crossing of several XRD peaks (or d-spacings).

Before discussing the pressure dependence of unit-cell parameters and volume in detail, we would like to comment on the peak broadening observed in XRD peaks beyond 10 GPa. This can be seen in Figs. 3 and S1, in particular for peaks (100), (120), and $(3\bar{4}1)$. This peak broadening is caused by the nonisotropic compression of $Zn(IO_3)_2$ which we have described above. The peaks we labeled as (101), (120), and (041) are in fact multiples corresponding to (021)/(101), $(1\bar{4}0)$/$(2\bar{2}0)$/(120), and (201)/$(2\bar{4}1)$/(041), respectively. Due to the anisotropic compression of $Zn(IO_3)_2$ the degeneracy of these multiples is broken around 10 GPa with the consequent peak broadening. We are aware that this phenomenon happens near the pressure where methanol-ethanol-water become a hard glass [24], and thus part of the broadening could be related to nonhydrostatic effects. However, since the conclusions we will report are supported by computer simulations (done under hydrostatic conditions) we consider that the phase transition we will report near 10 GPa is genuine, and not triggered by nonhydrostatic effects (or sample bridging).

Figure 4 shows the experimental and theoretical pressure dependence of the unit-cell volume of $Zn(IO_3)_2$. A continuous change of the experimental unit-cell volume of the monoclinic structure is found along the whole pressure range up to 28 GPa with no appreciable jump in volume at any pressure. A third-order Birch-Murnaghan (BM) [40,41] equation of state (EOS) was adopted to fit the volume within the whole pressure range. The bulk modulus is 21.6(0.7) and 18.4(1.5) GPa according to experiments and calculations and the corresponding pressure derivative is 7.0(0.3) and 6.7(0.7), respectively. Experiment and calculation describe a similar high-compressibility behavior of $Zn(IO_3)_2$ at low pressures and the minor difference between them is within a reasonable error [42]. However,

TABLE II. Calculated and measured zero-pressure frequencies (ω), pressure coefficients, and Grüneisen parameters of the Raman-active modes of $Zn(IO_3)_2$. Bulk moduli used to calculate Grüneisen parameters were obtained from our DFT-calculated and HP-XRD data. Results are compared with previous experiments [16,17].

	Theory ($B_0 = 18.4$ GPa)			Experiment ($B_0 = 21.6$ GPa)				
Mode	ω (cm^{-1})	$d\omega/dP$ (cm^{-1}/GPa)	γ	ω (cm^{-1})	$d\omega/dP$ (cm^{-1}/GPa)	γ	ω [17]	ω [16]
A	65.11	6.53	1.84	62	6.62	2.31	61	
B	68.35	1.06	0.28	67				
A	79.19	3.66	0.85	80	3.63	0.99	80	80
B	82.56	2.49	0.55					
A	101.30	2.07	0.38					
B	110.08	2.30	0.38	101	2.85	0.61	100	
A	117.58	11.84	1.85	111	8.60	1.67	111	113
B	130.82	6.62	0.93					
A	136.49	3.64	0.49	128	11.73	1.99	130	132
A	142.00	5.96	0.77	149			148	
B	148.24	2.43	0.30					
A	155.14	6.44	0.76					
B	165.41	8.50	0.95	156	3.71	0.51	155	152
A	171.85	6.49	0.70	173	7.28	0.91	173	173
B	173.82	5.64	0.60					
A	177.56	8.20	0.85					
B	178.19	6.34	0.65					
A	185.36	3.07	0.30					
B	193.47	6.39	0.61	187	7.54	0.87	187	189
A	196.60	10.48	0.98					
B	212.11	3.76	0.33					
A	212.35	0.96	0.08					
B	224.42	9.35	0.77					
B	237.16	9.88	0.77					
A	239.73	7.41	0.57					
B	243.07	8.52	0.64					
A	262.65	5.34	0.37	264	5.77	0.47	265	267
A	307.48	3.41	0.20					
B	309.88	4.45	0.26					
B	325.39	1.54	0.09	327	3.80	0.25	327	327
A	332.93	5.28	0.29					
A	337.63	4.90	0.27					
B	344.67	5.82	0.31	351	5.77	0.35	351	354
A	374.06	5.22	0.26					
B	375.29	3.13	0.15					
A	395.74	5.60	0.26	391	2.36	0.13	387	391
A	405.78	7.23	0.33	422	6.96	0.36	422	424
B	411.42	6.35	0.28					
B	428.70	5.74	0.25	432	10.06	0.50		
B	627.57	−6.90	−0.20	713			728	
A	656.22	−3.85	−0.11					
B	661.86	−9.36	−0.26					
A	666.36	−3.84	−0.11					
B	673.73	−6.06	−0.17	734	−2.93	−0.09	733	735
A	681.87	−5.62	−0.15					
A	688.54	−0.72	−0.02	757	−2.75	−0.08	756	760
A	715.60	−8.74	−0.22	782	−1.29	−0.04	781	782
B	727.77	−3.09	−0.08				796	
A	739.75	−0.85	−0.02					
B	755.66	−2.08	−0.05	817	−0.22	−0.01	815	815
B	767.03	2.02	0.05	840	7.79	0.20	838	836

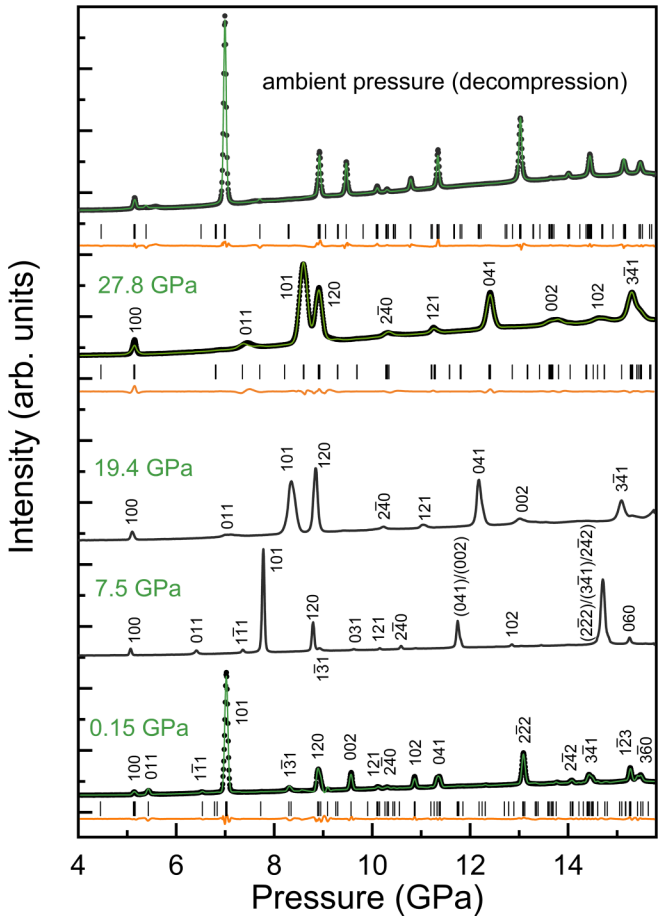

FIG. 3. Selected XRD patterns of $Zn(IO_3)_2$ under pressure. Bottom and top patterns show the refinement at the lowest pressures of the compression and decompression processes. Experimental data, refinement data, and residuals are plotted with dots, green and orange lines, respectively. The Bragg peak positions (black vertical lines) are also shown. A figure including more patterns can be found in the Supplemental Material (Fig. S1) [22].

the difference between experimental and calculated volumes becomes more pronounced as the pressure is increased, in opposition to the general systematic followed by oxides [42]. This could be a consequence of the formation of new I-O bonds under HP (as we will discuss later) which enhances localization of electronic states (in opposition to the electron delocalization induced by pressure in oxides). In this context, we must note that while our experimental data can be reasonably fitted to a single third-order EOS, our theoretical data do not fit nicely to a third-order EOS along the whole pressure range, especially between 3 and 10 GPa. This fact could be related to the occurrence of isosymmetric phase transitions in $Zn(IO_3)_2$, which will be discussed in the following paragraphs.

In our previous study [7], we summarized the bulk modulus of some metal iodates, including $Fe(IO_3)_3$ [7], $LiIO_3$ [9,10], KIO_3 [11], and $LiZn(IO_3)_3$ [43]. The bulk modulus of $Zn(IO_3)_2$ is equivalent to that of the ambient-pressure phase of KIO_3 [11], about two-thirds of that of $LiIO_3$ reported by our calculations [7] and Hu *et al.* [9], and two-fifths of that of the low-pressure phase of $Fe(IO_3)_3$ [7] and $LiZn(IO_3)_3$ [43].

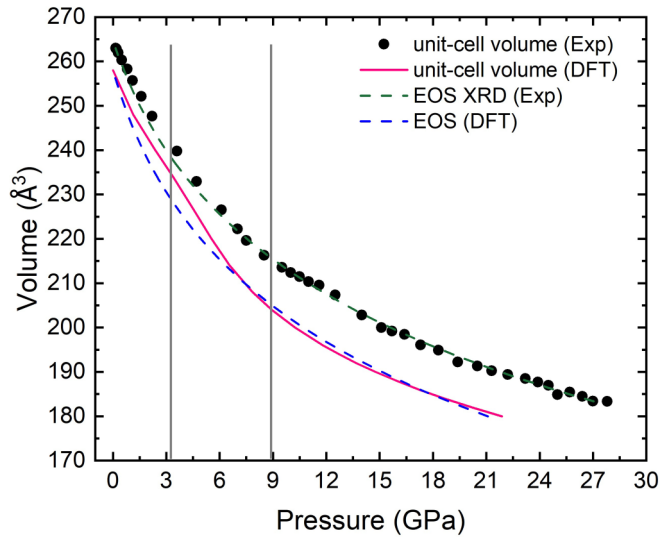

FIG. 4. Pressure dependence of the unit-cell volume. The black circles are the results of experiments and the magenta solid lines the results of calculations. The equations of state described in the text are shown with dashed lines. The vertical lines indicate the transition pressures.

Thus $Zn(IO_3)_2$ is one of the most compressible iodates, being as compressible as metal-organic frameworks [44] and group-XV oxides containing cationic LEPs [45,46], and having a bulk modulus only 30% larger than argon [47].

In order to further characterize volume changes, we have used a third-order BM EOS to describe the pressure dependence of the ZnO_6, I_1O_6, and I_2O_6 octahedral volumes (here we assume a 3+3 coordination of I). In this scenario, we obtain zero-pressure bulk moduli of 66(2), 21(2), and 20(2) GPa, with corresponding pressure derivatives of 4.2(0.5), 5.3(0.5), and 5.3(0.5), respectively. Since we already know that the bulk modulus of bulk $Zn(IO_3)_2$ is 21.6 GPa in the experiment and 18.4 GPa in the calculations, it is clear that the bulk modulus of the crystal is mainly determined by the compression of IO_6 units, rather than the compression of the ZnO_6 unit. This result is similar to what has been found in $Fe(IO_3)_3$ [7].

From Rietveld refinement of HP-XRD patterns, we have studied the evolution of unit-cell parameters of $Zn(IO_3)_2$ under pressure. To illustrate the quality of refinements we show them at 0.15 GPa, 27.8 GPa, and ambient pressure after decompression. The quality factors of Rietveld refinement are $R_p = 5.32\%$ and $R_{wp} = 7.19\%$ (0.15 GPa), $R_p = 5.86\%$ and $R_{wp} = 7.58\%$ (27.8 GPa), and $R_p = 5.48\%$ and $R_{wp} = 7.32\%$ (ambient pressure after decompression). Experimental results are compared with the results of DFT calculations in Fig. 5. There is an excellent agreement between experimental and theoretical results. Thus, we conclude that our calculations describe properly the crystal behavior under compression. As can be seen in Fig. 5, the behavior is strongly anisotropic. In addition, distinctive behaviors are observed for pressure ranges separated by vertical lines in Fig. 5 ($P < 3.4$ GPa, 3.4 GPa $< P <$ 8.9 GPa, $P >$ 8.9 GPa). In the low-pressure range, the linear compressibilities of *a*- and *b* axes are similar and very small. In the medium-pressure range, they are even negative. Finally, in the high-pressure range, both unit-cell

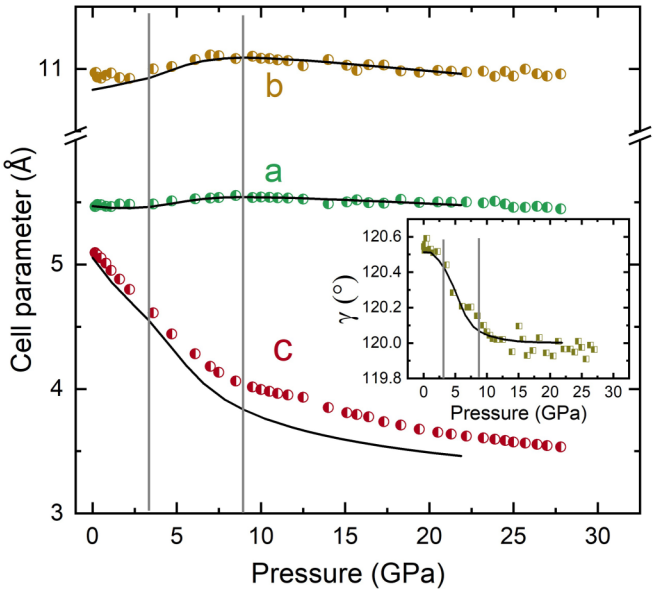

FIG. 5. Pressure dependence of the unit-cell parameters of $Zn(IO_3)_2$. The inset shows the evolution of the monoclinic angle γ. Half-filled circles or squares are the experimental data while DFT calculation results are shown in black solid lines.

parameters show a similar slow decrease with pressure. In contrast, the behavior of the c axis is very different, being much more compressible than the other two axes, at least in the two first pressure ranges, and showing a strong decrease of the compressibility in the third pressure range. The much higher compressibility of the c axis at low pressures is a consequence of the quasilayered structure formed by IO_3 polyhedra and connected by ZnO_6 octahedron along this direction (see Fig. 1). Note that the structure is not strictly layered because ZnO_6 octahedra connect alternate IO_3 layers; however, IO_3E units lead to considerable empty spaces in the structure along the c axis where the iodine LEPs are located. The collapse of the space between IO_3 layers contributes to the high compressibility of the c axis and favors the formation of three additional I-O bonds. In contrast, the alternate arrangement of the ZnO_6 octahedron and IO_3 tetrahedron along a- and b axes strengthen the force and resist compression along those directions.

To highlight the different behavior of the axes in $Zn(IO_3)_2$, we plot in Fig. S3 the ratio between lattice parameters as a function of pressure. It can be seen that the b/a ratio is almost insensitive to pressure, but b/c and a/c have a subtle slope change at 3.4 and a more drastic slope change at 8.9 GPa that agree with those observed in the lattice parameters and the monoclinic gamma angle, as commented below. These changes are more evident in experiments than in calculations, but are detected by both methods.

We will comment now on the pressure dependence of the monoclinic γ angle (inset of Fig. 5). Before doing that, we would like to mention that at the lowest pressure (0.15 GPa) we got an experimental γ angle of 120.5(1)°, which is slightly higher than the ambient pressure value [120.37(8)°] but comparable within error bars. Upon compression, we have found both an experimental and theoretical S-like nonlinear pressure dependence of the monoclinic angle γ that is related to the symmetry increase of ZnO_6 and IO_6 polyhedra under pressure, with changes of slope near 3.4 and 8.9 GPa, in good agreement with the changes observed in the lattice parameters.

Based upon the good agreement between calculations and experiments regarding the pressure dependence of structural parameters and the difficulty to obtain reliable atomic positions from our HP-XRD measurements due to the influence of preferred orientations, we have performed a more detailed analysis of the theoretical data to investigate the behavior of the monoclinic structure near 3.4 and 8.9 GPa. In particular, we have used those data to calculate the pressure dependence of the theoretical distortion index $D = \frac{1}{n}\sum \frac{|l_i - l_{av}|}{l_{av}}$ (where n is the number of bonds, l_i is the distance from the central atom to the i th coordinating atom, and l_{av} is the average bond length) [48] of both polyhedra as calculated by using VESTA [49] (see Fig. S4 in the Supplemental Material [22]). The decrease of the distortion index of both polyhedra upon compression suggests a symmetry increase of both polyhedra under pressure. An almost linear decrease of the distortion index of IO_6 units is observed. Additionally, an S-like nonlinear decrease of the distortion index of ZnO_6 units with changes in slopes near 3.8 and 8.9 GPa are observed. The sum of the pressure effect on both polyhedra causes the nonlinear change of γ under pressure. Moreover, the changes observed in both polyhedra lead to: (i) a symmetrization of the ZnO_6 octahedron, and (ii) the gradual formation of IO_6 octahedra; i.e., an increase of I coordination due to the rapid decrease of the second-nearest neighbor I-O distances (represented in dashed lines in Fig. 1). These are evidence of the anisotropic compression of $Zn(IO_3)_2$. We will comment more on this unusual behavior below when talking about the behavior of Zn-O and I-O distances.

We think the structural changes observed at 3.4 and 8.9 GPa are caused by two subtle isostructural phase transitions [50,51] (understood as transitions between two phases having the same space group, involving subtle changes in cell dimensions and changes in polyhedral coordination). More evidence of the existence of the two IPTs is shown in Figs. S5–S13 in the Supplemental Material [22], where the pressure dependence of the theoretical atomic coordinates of Zn, I, and O atoms are presented. Just as an example, we will comment on the calculated y atomic coordinate of Zn (see Fig. S5). Its initial value 0.7460 decreases sharply to 0.7452 at 2.5 GPa, and then increases to 0.7482 at 8.9 GPa; above this pressure, there is a sudden slope change, increasing slowly to 0.7488 at 21.9 GPa. The whole picture of the evolution is nonlinear having an S-like shape. A similar S-like evolution of the atomic positions can be seen also in other atoms, thus supporting the two IPTs already commented.

More evidence for the two IPTs can be found in the theoretical pressure dependence of the Zn-O and I-O distances and, more importantly, in the experimental and calculated Raman-mode evolution under pressure to be discussed in the next section. Regarding the pressure dependence of the Zn-O distances (see Fig. 6), one can notice an unusual S-like behavior for most Zn-O bond distances, except for Zn–O_3. The behavior of the three short Zn-O bonds is consistent with the proposed IPTs at 3.4 and 8.9 GPa, with a decrease of the bond distances up to 3.8 GPa, an increase above this pressure

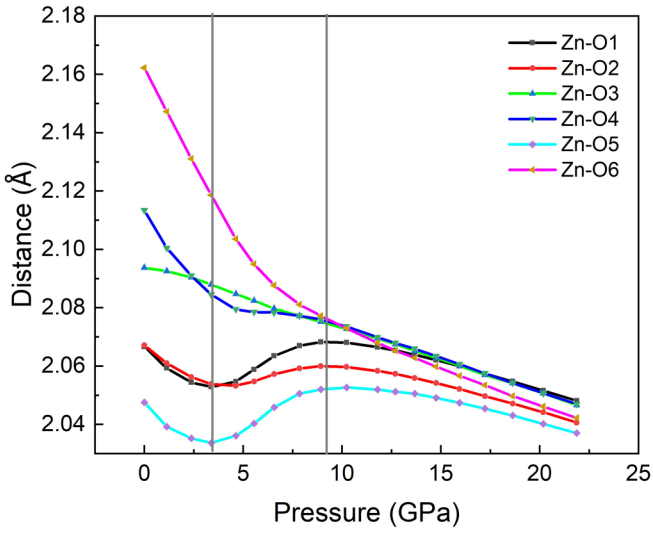

FIG. 6. Pressure dependence of the theoretical Zn-O bond distances.

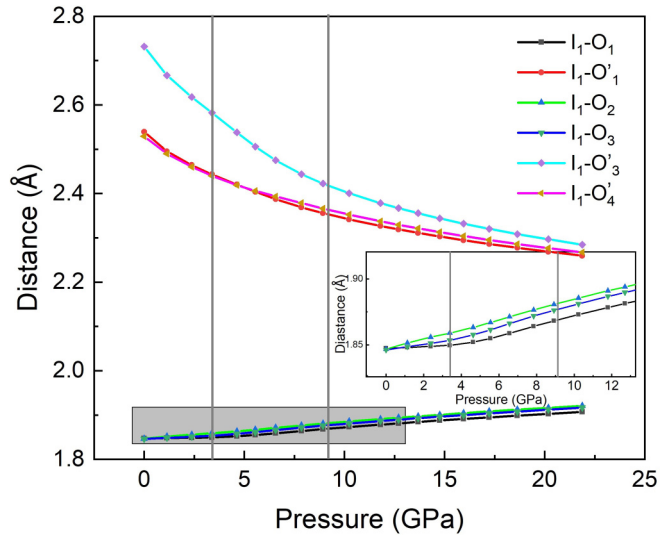

FIG. 7. Pressure dependence of the theoretical I-O bond distances. The inset shows a zoom of the I-O_1, I-O_2, and I-O_3 distances below 13 GPa. O' is used for second-neighbor oxygen atoms.

and up to 8.9 GPa followed by a new decrease above this pressure. We can observe a considerable decrease of the three longest Zn-O bond distances to achieve an almost regular ZnO_6 polyhedron above 9.8 GPa, as already pointed out by the polyhedral distortion (Fig. S4).

As regards the pressure dependence of the I-O distances, we must recall that there are two different atomic positions for iodine, I_1, and I_2 (see Fig. 1 and Table S1 in Supplemental Material [22]). Each type of iodine atom is shown with a different color in Fig. 1. However, both coordination polyhedra are extremely similar. For instance, I_1-O distances are 1.8474, 1.8466, and 1.8462 Å at ambient pressure and I_2-O distances are 1.8475, 1.8452, and 1.8447 Å, behaving both polyhedral similarly under compression; indeed, their compressibility is very similar as commented before. Thus for the sake of briefness, here we will focus on the change of I_1-O bond distances with pressure (Fig. 7). As observed, for the I_1 atom there are three short I-O distances (I_1-O_1, I_1-O_2, and I_1-O_3) and three large distances above 2.5 Å at room pressure (I_1-O'_1, I_1-O'_3, and I_1-O'_4, which correspond to second neighbors; primes are used to identify second neighbors). In the IO_6 polyhedron, these three second-neighbor O atoms show distances above 2.5 Å and are not forming a bond with I at low pressure. As pressure increases, these long distances show a strong decrease and gradually form new bonds. We can find a gradual I coordination change if we choose 2.48 Å as the maximum bonding distance (a value 25% larger than the shortest I-O distance). [52]. In this way, with increasing pressure, O'_1, O'_3,, and O'_4, which is on the side of the iodine LEPs, approaches I_1, first forming new I-O bonds with iodine at around 2.5 GPa, and then the I atom becomes sixfold coordinated above around 8 GPa due to the decrease of the I-O'_3 distance. On the other hand, at ambient pressure, the ZnO_6 octahedron is more symmetrical than the IO_6 octahedron, and compared with the change in the bond distance between Zn and O under pressure (the largest change is the change in the bond distance between the Zn and O_6 atoms, from 2.16 to 2.04 Å, 5.6% reduction), the change of the bond distance between I and O is in a larger range; the biggest change is the bond distance change between I and O_3 atom, shortened from 2.73 to 2.28 Å, a decrease of 16.5%. The great compressibility of the three longest I_1-O bond distances compared to the Zn-O bonds and the three shortest I-O bonds (Fig. 7) make the IO_6 octahedron to have a much larger compressibility than the ZnO_6 octahedron, as already commented.

The strong distortion of the IO_6 polyhedra at low pressures is due to the large stereoactivity of the iodine LEP. This stereoactivity decreases in strength with pressure and ultimately disappears in order to stablish the three new bonds above around 8 GPa, thus leading to a more regular IO_6 polyhedron as already commented. The pressure-induced reduction of the cation LEP stereoactivity can be found in some other materials, like $Fe(IO_3)_3$ [6,7], $SbPO_4$ [53], and As_2S_3 [54]. On the other hand, we must say that the I_1–O_1 bond distance clearly shows a different pressure dependence before and after 3.4 GPa, thus supporting also the existence of an IPT around that pressure (see inset of Fig. 7).

Finally, we must note that there is an increase of the three shortest I-O distances that is in contrast to the decrease in the three largest I-O distances. The increase of the three shortest I-O distances will lead to the soft behavior of some Raman-active modes at HP that we will show in the next section. In this context, it must be stressed that an increase of the three shorter Zn-O bond distances with increasing pressure have also been observed between 3.8 and 8.9 GPa. The *S*-like behavior of the Zn-O bond distances with pressure is not normal. In particular, the increment of the cation–anion bond distance and the equalization of the different bond distances has been recently observed for As–S bonds in orpiment (As_2S_3) under compression [54]. In that case, it was ascribed to the formation of a new type of bond, named metavalent bonding, and ascribed to the sharing of electrons of two covalent As-S bonds (with 2 electrons per bond) in order to form 5 metavalent bonds (with 1 electron per bond). Therefore, we

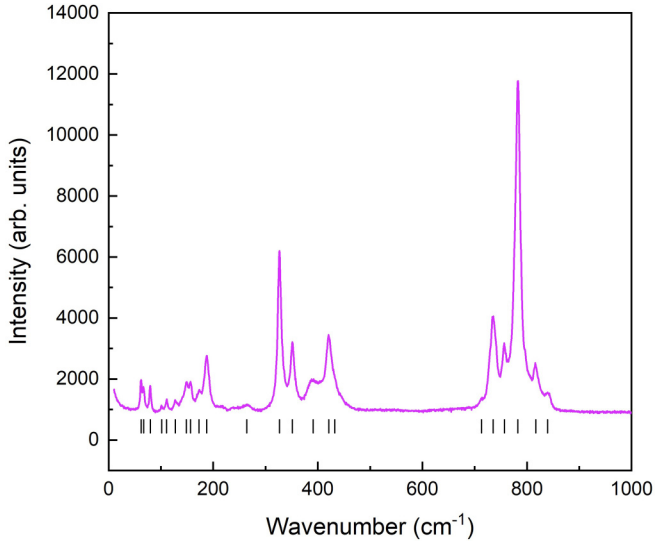

FIG. 8. Raman spectra of $Zn(IO_3)_2$ at ambient conditions. The determined peak position is indicated by ticks.

tentatively ascribe the *S*-like behavior of Zn-O bond distances to the competition of two effects that should be investigated in further works.

B. Raman study

First, we will start discussing the Raman spectra of $Zn(IO_3)_2$ at ambient pressure (see Fig. 8). The RS spectrum at ambient pressure is very similar to those reported in the literature [16,17]. It can also be mentioned that the Raman spectrum of $Zn(IO_3)_2$ bears some resemblance to that of $Fe(IO_3)_3$ [6], despite the different crystal structures of the two compounds. In particular, all of them have Raman-active modes distributed in two isolated regions separated by a phonon gap, one high-frequency region for wave numbers larger than 700 cm^{-1} and the other one for wave numbers smaller than 450 cm^{-1}. In fact, the lowest region can be subdivided into two regions, a low-frequency region below 200 cm^{-1} and a medium-frequency region between 200 and 450 cm^{-1}. The strongest mode is always in the high-frequency region. In this paper, we will show that the high-frequency modes can be linked to internal I-O vibrations (stretching and bending) inside the IO_6 polyhedra. In particular, the strongest mode is related to a symmetric stretching I-O vibration.

According to group theory, $Zn(IO_3)_2$ should have 54 vibrational modes with 3 acoustic modes ($A + 2B$) and 51 Raman-active and IR modes ($26A+25B$). We have observed 22 Raman-active modes out of 51. In previous studies, 21 and 16 modes have been reported [16,17]. Our results and those of previous works show a nice agreement (see Table II). The calculated frequencies for all these modes together with a tentative mode assignment are also provided in Table II. We must note that the experimental mode assignment in Table II is based on comparing the experimental frequencies at ambient pressure and their pressure coefficients at different pressure ranges with those obtained from DFT calculations. The agreement between experiments and calculations is similar to that found in $Fe(IO_3)_3$ [6]. The strongest Raman modes

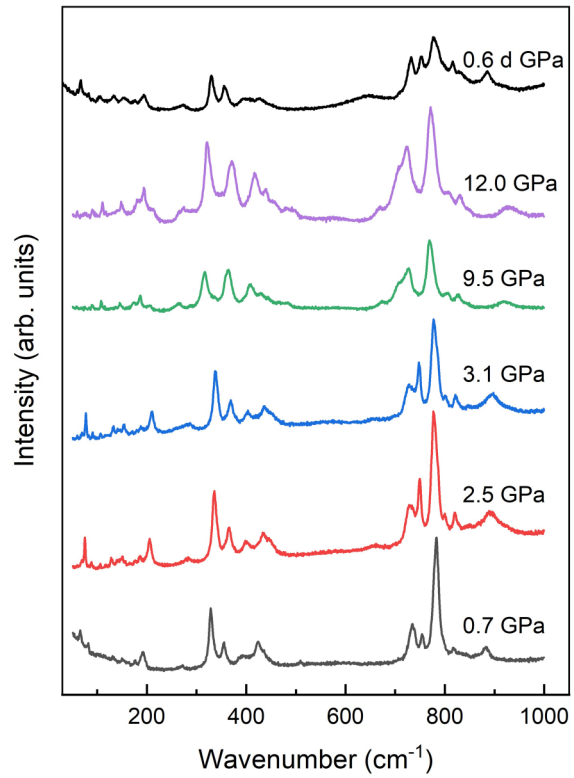

FIG. 9. Selected Raman spectra of $Zn(IO_3)_2$ under pressure. Pressure are indicated and "d" means decompression.

in $Zn(IO_3)_2$ and $Fe(IO_3)_3$ are at 782 and 790 cm^{-1}, respectively [6]. Indeed, this mode has been attributed to an *A* mode corresponding to the symmetric I-O stretching mode inside IO_3 units. Since I-O distances are very similar in both iodates, it is expected that both modes should have a similar frequency.

Now we focus on the HP behavior of the RS spectra in $Zn(IO_3)_2$ to continue our discussion (see Fig. 9). A change in the intensity of some modes is observed as pressure increases. For instance, the peak around 200 cm^{-1} at 0.7 GPa is barely followed above 9 GPa. In addition, some peaks merge into one broad peak, like what happened to the soft mode of the high-frequency region around 720 cm^{-1} at 0.7 GPa. In addition, we can observe two features in the RS spectra of $Zn(IO_3)_2$ under pressure that are similar to those reported in $Fe(IO_3)_3$ [6]: (i) A reversible change of the HP-RS spectra, and (ii) a closing of the phonon gap between the medium- and high-frequency regions.

The pressure evolution of the Raman-mode frequencies and the closing phonon gap can be better seen in Fig. 10. In the medium- and low-frequency regions, there is a close agreement between experimental and theoretical results. Under compression, there are some crossings and anticrossings of modes but all vibrational modes correspond to a monoclinic crystal structure described by space group $P2_1$ up to 12 GPa. In the high-frequency region ([Fig. 10 (c)], the behavior of the experimental modes can be described closely by calculations if we consider that theoretical calculations underestimate the experimental frequencies by ca. 70 cm^{-1}. This is a typical feature of DFT-GGA calculations [53], which tend to underestimate the restoring forces of internal modes. All the phonons

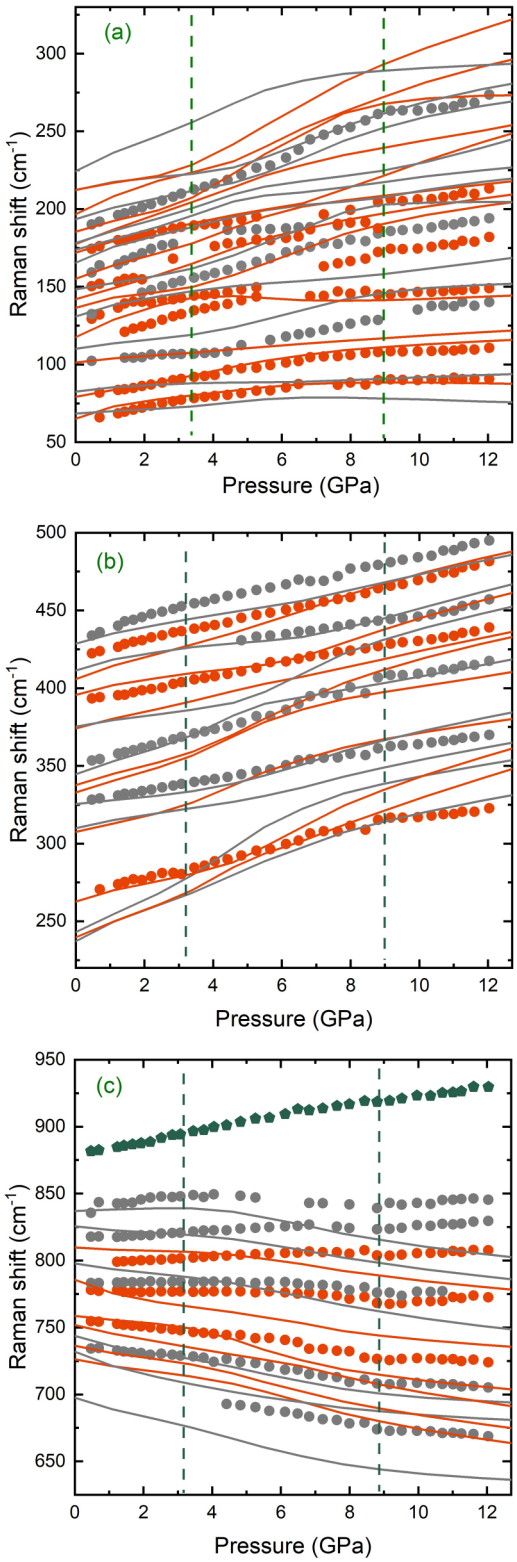

FIG. 10. Pressure dependence of experimental (symbols) and theoretical (lines) Raman-active modes of $Zn(IO_3)_2$. (a)–(c) show different wave-number regions. A tentative mode assignment of the experimental data is show with different colors: Red and gray colors are used for A and B modes, respectively. In (c), we shifted all calculated modes by $+70\,cm^{-1}$, in order to facilitate the comparison with experiments.

were fitted by a quadratic equation using the data below 3 GPa due to the S-like behavior of the mode evolution curve and the zero-pressure coefficients and Grüneisen parameters can be found in Table II. The nonlinear S-like curve, which can be found in the evolution of almost all the experimental and calculated modes (see Fig. 10 and Fig. S14 in Supplemental Material for a selection of modes highlighting the phenomenon), is a result of the two symmetry-preserving IPTs. The vertical dashed green line indicated the phase transition pressure in HP-RS measurements, which is in excellent agreement with what we found in HP-XRD measurements. The nonlinear pressure dependence of the Raman-active mode frequencies, related to IPTs, can also be found in $Fe(IO_3)_3$ [6].

Now we focus on the high-frequency region of the Raman spectrum [see Fig. 10(c)]. First, we would like to mention that the experimental mode of highest frequency is a second-order Raman mode that is likely a combination of modes observed near 400–450 cm^{-1} (all of them showing positive pressure coefficient). Second, we would like to comment on the observed phonon softening upon compression of many high-frequency modes. This is a common feature of all the calculated phonons and most experimental phonons of $Zn(IO_3)_2$. Based on our DFT calculation, we are capable of seeing the related atomic movements of all phonons by using J-ICE [55] and in particular, those corresponding to the high-frequency soft phonons (see Fig. S15 in the Supplemental Material [22]). The soft phonons in our experimental data are mostly related to the stretch of the short I-O bonds, and the cause of the soft behavior of those phonons is the decrease of the force of these bonds as pressure increases due to the increase of the short I-O distances as pressure increases (see Fig. 7) as suggested by our DFT calculations.

To verify the hypothesis of the softening of the high-frequency phonons due to the increase of the short I-O bonds, we have assumed under a harmonic approximation that the force constant, k, of the I-O bond is a function of negative cubic of the average I-O bond distance, $(d_{I\text{-}O})^{-3}$. Since the frequency of the stretching mode, ω, can be written as $\omega = (k/\mu)^{1/2}$, where μ is the reduced mass, if the assumption is right and the mode softening is caused by the increase of the bond distance, then we can find a linear relationship between $\omega^{-2/3}$ and the bond distance. By using the calculated data, we plotted the theoretical frequencies of the soft modes with the average I-O bond distance in IO_3 units (see Fig. 11). We do see a clear linear relationship between the frequency and average I-O bond distance; thus, the occurrence of the soft mode at the high-frequency region is induced by the increase of the three shortest I-O bond distances, which, as we explained before, is needed to accommodate the additional O atoms around iodine as pressure increases. The same HP behavior of the IO_3 units has been found in $Fe(IO_3)_3$ so it seems to be a common feature of compounds with iodine LEPs. We have to note that the softening of phonons related to the increase of short bonds with pressure has been also recently found in mineral orpiment (As_2S_3) and explained in the context of the formation of metavalent bonding at HP in compounds with stereoactive LEPs [54]. To explore this hypothesis in $Zn(IO_3)_2$ new studies are needed.

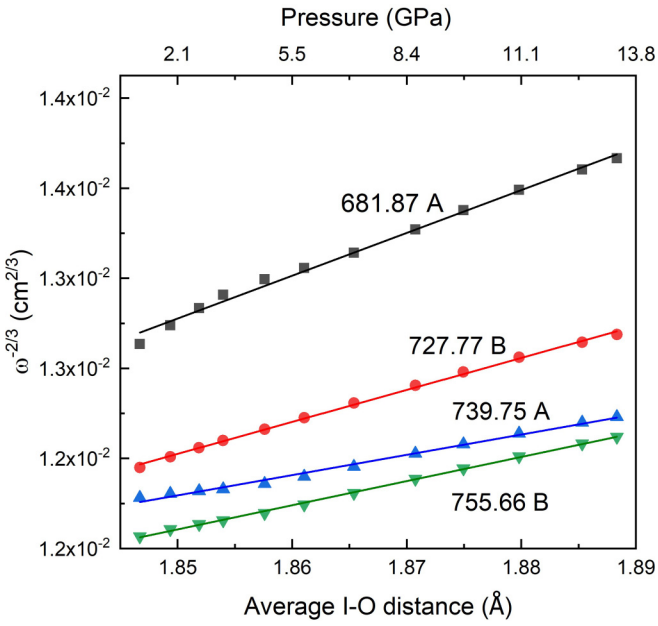

FIG. 11. Relationship between average I-O bonds and the theoretical $\omega^{-2/3}$ for some soft Raman-active modes of $Zn(IO_3)_2$. The corresponding atomic movement of each mode can be found in Fig. S15 [22]. In the upper axis the pressure of each average bond is indicated.

IV. CONCLUSIONS

HP-XRD and HP-RS measurements were used to study the HP behavior of $Zn(IO_3)_2$ along with DFT theoretical calculations. The monoclinic crystal structure shows a high anisotropy and the most compressible axis is the *c* axis. With a bulk modulus $B_0 = 21.6$ GPa, $Zn(IO_3)_2$ is the most compressible one among the whole reported metal iodine family. The compressibility of $Zn(IO_3)_2$ is governed by the compressibility of the IO_6 units. The symmetry of the experimental Raman-active modes was tentatively assigned and the softened phonons found at the high-frequency region were related to the increase of the shortest I-O bonds under pressure.

Two reversible symmetry-preserving IPTs were found and located around 2.5–3.4 and 8–9 GPa, without change of the space-group symmetry or crystal volume collapse. The two IPTs are associated with a gradual change from threefold to sixfold of the I coordination under pressure, despite the fact that most notable changes at the two pressure ranges are found for the *y* atomic coordinate of the Zn atom. The presence of the two IPTs leads to a nonlinear *S*-like pressure dependence of the unit-cell lattice parameters and Raman-active modes upon compression in both experiments and theoretical calculations, as well as in the calculated Zn–O and I-O bond distances. The gradual increase of I coordination with pressure due to the decrease of the large I-O bonds followed by an increase of the short I-O distances could be indicative of the formation of metavalent bonding at HP in compounds with stereoactive LEPs, as recently suggested for orpiment. To explore this hypothesis further studies are needed.

ACKNOWLEDGMENTS

This work was supported by the Spanish Ministry of Science, Innovation and Universities under Grants No. PID2019-106383GB-C41/42/43 and No. RED2018-102612-T (MALTA Consolider-Team Network) and by Generalitat Valenciana under Grant No. Prometeo/2018/123 (EFIMAT). A.L. and D.E. would like to thank the Generalitat Valenciana for the Ph.D. Fellowship No. GRISOLIAP/2019/025). C.P. is thankful for the financial support of the Spanish Mineco Project No. FIS2017-83295-P. Powder x-ray diffraction-experiments were performed at the Materials Science and Powder Diffraction beamline of ALBA Synchrotron (Alba Experiment No. 2019083663). Z.H. sincerely thanks Professor I. K. Lefkaier – Laboratoire Physique des Matériaux (LPM) University of Laghouat Algeria – for the support and fruitful discussions.

[1] J. G. Bergman, G. D. Boyd, A. Ashkin, and S. K. Kurtz, New nonlinear optical materials: Metal oxides with nonbonded electrons, J. Appl. Phys. **40**, 2860 (1969).

[2] C. Wang, T. Zhang, and W. Lin, Rational synthesis of noncentrosymmetric metal-organic frameworks for second-order nonlinear optics, Chem. Rev. **112**, 1084 (2012).

[3] K. M. Ok, E. O. Chi, and P. S. Halasyamani, Bulk characterization methods for non-centrosymmetric materials: Second-harmonic generation, piezoelectricity, pyroelectricity, and ferroelectricity, Chem. Soc. Rev. **35**, 710 (2006).

[4] A. K. Sagotra, D. Errandonea, and C. Cazorla, Mechanocaloric effects in superionic thin films from atomistic simulations, Nat. Commun. **8**, 963 (2017).

[5] C. Cazorla, Novel mechanocaloric materials for solid-state cooling applications, Appl. Phys. Rev. **6**, 041316 (2019).

[6] A. Liang, S. Rahman, P. Rodriguez-Hernandez, A. Muñoz, F. J. Manjón, G. Nenert, and D. Errandonea, High-pressure Raman study of $Fe(IO_3)_3$: Soft-mode behavior driven by coordination changes of iodine atoms, J. Phys. Chem. C **124**, 21329 (2020).

[7] A. Liang, S. Rahman, H. Saqib, P. Rodriguez-Hernandez, A. Munoz, G. Nenert, I. Yousef, C. Popescu, and D. Errandonea, First-order isostructural phase transition induced by high-pressure in $Fe(IO_3)_3$, J. Phys. Chem. C **124**, 8669 (2020).

[8] J. Liu, Z. Shen, Y. Zhang, X. Yin, and S. He, The P-T phase diagram of lithium iodate (LiIO3) up to 40 Kbars, Acta Phys. Sin **32**, 118 (1983).

[9] J. Hu, L. Chen, L. Wang, R. Tang, and R. Che, Isothermal compression of α-$LiIO_3$ and its phase transition under high pressure and high temperature, Acta Phys. Sin. **36**, 1099 (1987).

[10] W. W. Zhang, Q. L. Cui, Y. W. Pan, S. S. Dong, J. Liu, and G. T. Zou, High-pressure x-ray diffraction study of $LiIO_3$ to 75 GPa, J. Phys.: Condens. Matter **14**, 10579 (2002).

[11] L. Bayarjargal, L. Wiehl, A. Friedrich, B. Winkler, E. A. Juarez-Arellano, W. Morgenroth, and E. Haussühl, Phase transitions in KIO_3, J. Phys.: Condens. Matter **24**, 325401 (2012).

[12] Y. Suffren, I. Gautier-Luneau, C. Darie, C. Goujon, M. Legendre, and O. Leynaud, First evidence of a phase transition

in a high-pressure metal iodate: Structural and thermal studies of $AgIO_3$ polymorphs, Eur. J. Inorg. Chem. **2013**, 3526 (2013).

[13] G. J. Shanmuga Sundar, S. M. R. Kumar, M. Packiya raj, and S. Selvakumar, Synthesis, growth, optical, mechanical and dielectric studies on NLO active monometallic zinc iodate [$Zn(IO_3)_2$] crystal for frequency conversion, Mater. Res. Bull. **112**, 22 (2019).

[14] D. Phanon, B. Bentria, E. Jeanneau, D. Benbertal, A. Mosset, and I. Gautier-Luneau, Crystal structure of $M(IO_3)_2$ metal iodates, twinned by pseudo-merohedry, with MII: MgII, MnII, CoII, NiII and ZnII, Z. Kristallogr. **221**, 635 (2006).

[15] J. K. Liang and C. G. Wang, The structure of $Zn(IO_3)_2$ crystal, Acta Chim. Sin. **40**, 985 (1982).

[16] T. C. Kochuthresia, I. Gautier-Luneau, V. K. Vaidyan, and M. J. Bushiri, Raman and FTIR spectral investigations of twinned $M(IO_3)_2$ (M = Mn, Ni, Co, AND Zn) crystals, J. Appl. Spectrosc. **82**, 941 (2016).

[17] S. Peter, G. Pracht, N. Lange, and H. D. Lutz, Zinkiodate–schwingungsspektren (IR, Raman) und kristallstruktur von $Zn(IO_3)_2 \cdot 2H_2O$, Z. Anorg. Allg. Chem. **626**, 208 (2000).

[18] E. J. Skoug and D. T. Morelli, Role of Lone-Pair Electrons in Producing Minimum Thermal Conductivity in Nitrogen-Group Chalcogenide Compounds, Phys. Rev. Lett. **107**, 235901 (2011).

[19] M. D. Nielsen, V. Ozolins, and J. P. Heremans, Lone pair electrons minimize lattice thermal conductivity, Energy Environ. Sci. **6**, 570 (2013).

[20] A. Benghia, Z. Hebboul, R. Chikhaoui, I. khaldoun Lefkaier, A. Chouireb, and S. Goumri-Said, Effect of iodic acid concentration in preparation of zinc iodate: Experimental characterization of $Zn(IO_3)_2$, and its physical properties from density functional theory, Vacuum **181**, 109660 (2020).

[21] H. M. Rietveld, A profile refinement method for nuclear and magnetic structures, J. Appl. Crystallogr. **2**, 65 (1969).

[22] See Supplemental Material at http://link.aps.org/supplemental/10.1103/PhysRevB.103.054102 for structural information, additional x-ray diffraction patterns, additional information on structural analysis and Raman experiments results, a description of atomic movements associated to phonons, and results from density-functional theory calculations.

[23] A. Dewaele, P. Loubeyre, and M. Mezouar, Equations of state of six metals above 94 GPa, Phys. Rev. B **70**, 094112 (2004).

[24] S. Klotz, J. C. Chervin, P. Munsch, and G. Le Marchand, Hydrostatic limits of 11 pressure transmitting media, J. Phys. D: Appl. Phys. **42**, 075413 (2009).

[25] F. Fauth, I. Peral, C. Popescu, and M. Knapp, The new material science powder diffraction beamline at ALBA synchrotron, Powder Diffraction **28**, S360 (2013).

[26] H. K. Mao, J. Xu, and P. M. Bell, Calibration of the ruby pressure gauge to 800 Kbar under quasi-hydrostatic conditions, J. Geophys. Res. **91**, 4673 (1986).

[27] K. Nassau, J. W. Shiever, and B. E. Prescott, Transition metal iodates. I. Preparation and characterization of the 3d iodates, J. Solid State Chem. **7**, 186 (1973).

[28] D. Errandonea, A. Muñoz, and J. Gonzalez-Platas, Comment on "High-pressure x-ray diffraction study of YBO_3/Eu^{3+}, $GdBO_3$, and $EuBO_3$: Pressure-induced amorphization in $GdBO_3$" [J. Appl. Phys. 115, 043507 (2014)], J. Appl. Phys. **115**, 216101 (2014).

[29] G. Kresse and J. Hafner, Ab initio molecular dynamics for liquid metals, Phys. Rev. B **47**, 558 (1993).

[30] G. Kresse and J. Hafner, Ab initio molecular-dynamics simulation of the liquid-metalamorphous- semiconductor transition in germanium, Phys. Rev. B **49**, 14251 (1994).

[31] G. Kresse and J. Furthmüller, Efficiency of ab-initio total energy calculations for metals and semiconductors using a plane-wave basis set, Comput. Mater. Sci. **6**, 15 (1996).

[32] G. Kresse and J. Furthmüller, Efficient iterative schemes for ab initio total-energy calculations using a plane-wave basis set, Phys. Rev. B **54**, 11169 (1996).

[33] P. Hohenberg and W. Kohn, Inhomogeneous electron gas, Phys. Rev. **136**, B864 (1964).

[34] P. E. Blöchl, Projector augmented-wave method, Phys. Rev. B **50**, 17953 (1994).

[35] G. Kresse and D. Joubert, From ultrasoft pseudopotentials to the projector augmented-wave method, Phys. Rev. B **59**, 1758 (1999).

[36] J. P. Perdew, A. Ruzsinszky, G. I. Csonka, O. A. Vydrov, G. E. Scuseria, L. A. Constantin, X. Zhou, and K. Burke, Restoring the Density-Gradient Expansion for Exchange in Solids and Surfaces, Phys. Rev. Lett. **100**, 136406 (2008).

[37] H. J. Monkhorst and J. D. Pack, Special points for Brillouin-zone integrations, Phys. Rev. B **13**, 5188 (1976).

[38] A. Togo, F. Oba, and I. Tanaka, First-principles calculations of the ferroelastic transition between rutile-type and $CaCl_2$-Type SiO_2 at high pressures, Phys. Rev. B: Condens. Matter Mater. Phys. **78**, 134106 (2008).

[39] D. Díaz-Anichtchenko, D. Santamaria-Perez, T. Marqueño, J. Pellicer-Porres, J. Ruiz-Fuertes, R. Ribes, J. Ibañez, S. N. Achary, C. Popescu, and D. Errandonea, Comparative study of the high-pressure behavior of ZnV_2O_6, $Zn_2V_2O_7$, and $Zn_3V_2O_8$, J. Alloys Compd. **837**, 155505 (2020).

[40] F. D. Murnaghan, The compressibility of media under extreme pressures, Proc. Natl. Acad. Sci. U.S.A. **30**, 244 (1944).

[41] F. Birch, Finite elastic strain of cubic crystals, Phys. Rev. **71**, 809 (1947).

[42] B. Winkler and V. Milman, Density functional theory based calculations for high pressure research, Z. Kristallogr. **229**, 112 (2014).

[43] Z. Hebboul, C. Galez, D. Benbertal, S. Beauquis, Y. Mugnier, A. Benmakhlouf, M. Bouchenafa, and D. Errandonea, Synthesis, characterization, and crystal structure determination of a new lithium zinc iodate polymorph $LiZn(IO_3)_3$, Crystals **9**, 464 (2019).

[44] J. Navarro-Sánchez, I. Mullor-Ruíz, C. Popescu, D. Santamaría-Pérez, A. Segura, D. Errandonea, J. González-Platas, and C. Martí-Gastaldo, Peptide metal-organic frameworks under pressure: Flexible linkers for cooperative compression, Dalton Trans. **47**, 10654 (2018).

[45] A. L. J. Pereira, L. Gracia, D. Santamaría-Pérez, R. Vilaplana, F. J. Manjón, D. Errandonea, M. Nalin, and A. Beltrán, Structural and vibrational study of cubic Sb_2O_3 under high pressure, Phys. Rev. B **85**, 174108 (2012).

[46] A. L. J. Pereira, D. Errandonea, A. Beltrán, L. Gracia, O. Gomis, J. A. Sans, B. García-Domene, A. Miquel-Veyrat, F. J. Manjón, A. Muñoz, and C. Popescu, Structural study of α-Bi_2O_3 under pressure, J. Phys.: Condens. Matter **25**, 475402 (2013).

[47] D. Errandonea, R. Boehler, S. Japel, M. Mezouar, and L. R. Benedetti, Structural transformation of compressed solid Ar: An x-ray diffraction study to 114 GPa, Phys. Rev. B **73**, 092106 (2006).

[48] W. H. Baur, The geometry of polyhedral distortions. Predictive relationships for the phosphate group, Acta Crystallogr. B **30**, 1195 (1974).

[49] K. Momma and F. Izumi, VESTA 3 for three-dimensional visualization of crystal, volumetric and morphology data, J. Appl. Crystallogr. **44**, 1272 (2011).

[50] N. Boccara, Second-order phase transitions characterized by a deformation of the unit cell, Ann. Phys. (N. Y). **47**, 40 (1968).

[51] M. T. Dove, Theory of displacive phase transitions in minerals, Am. Mineral. **82**, 213 (1997).

[52] A. Krapp, F. M. Bickelhaupt, and G. Frenking, Orbital overlap and chemical bonding, Chem. - Eur. J. **12**, 9196 (2006).

[53] A. L. D. J. Pereira, D. Santamariá-Pérez, R. Vilaplana, D. Errandonea, C. Popescu, E. L. Da Silva, J. A. Sans, J. Rodríguez-Carvajal, A. Munõz, P. Rodríguez-Hernández, A. Mujica, S. E. Radescu, A. Beltrán, A. Otero-De-La-Roza, M. Nalin, M. Mollar, and F. J. Manjón, Experimental and theoretical study of $SbPO_4$ under Compression, Inorg. Chem. **59**, 287 (2020).

[54] V. P. Cuenca-Gotor, J. Á. Sans, O. Gomis, A. Mujica, S. Radescu, A. Muñoz, P. Rodríguez-Hernández, E. L. Da Silva, C. Popescu, J. Ibañez, R. Vilaplana, and F. J. Manjón, Orpiment under compression: metavalent bonding at high pressure, Phys. Chem. Chem. Phys. **22**, 3352 (2020).

[55] P. Canepa, R. M. Hanson, P. Ugliengo, and M. Alfredsson, J-ICE: A new Jmol interface for handling and visualizing crystallographic and electronic properties, J. Appl. Crystallogr. **44**, 225 (2011).